

# We are IntechOpen, the world's leading publisher of Open Access books Built by scientists, for scientists

6,900

Open access books available

186,000

International authors and editors

200M

Downloads

Our authors are among the

154

Countries delivered to

TOP 1%

most cited scientists

12.2%

Contributors from top 500 universities



WEB OF SCIENCE™

Selection of our books indexed in the Book Citation Index  
in Web of Science™ Core Collection (BKCI)

Interested in publishing with us?  
Contact [book.department@intechopen.com](mailto:book.department@intechopen.com)

Numbers displayed above are based on latest data collected.  
For more information visit [www.intechopen.com](http://www.intechopen.com)



## Development of Superlattice Infrared Photodetectors

Shih-Hung Lin, Ying-Hsiang Wang, Che-Wei Chang,  
Jen-Hsiang Lu, Chun Chi Chen and Chieh-Hsiung Kuan,  
*Department of Electrical Engineering, National Taiwan University  
Taipei, 10617 Taiwan, Republic of China*

### 1. Overview and Perspective

Infrared (IR) detectors play a critical role in both military and civilian applications and have been widely researched in recent decade. Because the atmospheric transparent windows for the IR radiation exist within the spectral ranges of 3–5 and 8–12  $\mu\text{m}$ , and the spectrum of the black-body radiation at room temperature has a peak at 10  $\mu\text{m}$ , the detectors with the 8–12  $\mu\text{m}$  detection spectra are helpful to identify the heat radiation from a target at room temperature. Such detectors are the research focus in this chapter.

The employment of intersubband transitions for the infrared radiation detection has drawn much attention. The transition is completed by the electrons which absorb photons with the appropriate energy equal to the subband energy difference to transit from the low subband to the high one. The intersubband photodetectors can be made from semiconductor heterostructures of multiple quantum wells (West & Eglash, 1985) (Harwit & Harris Jr., 1987) (Levine et al., 1987) or superlattices as shown in Fig. 1. Infrared detection will be done by the intersubband transitions between two quantum states in the multiple quantum wells or two minibands in the superlattices. The wells are sandwiched by thick barriers in the multiple quantum well structure. Therefore electron wavefunctions in the wells would not interact with each others and discrete quantum states are formed. Contrarily, the adjacent wells in the superlattice are separated by thin barriers. Minibands are formed in the superlattice region by the coupling of electron wavefunctions.

As shown in Fig. 1, in comparison with the quantum well infrared photodetectors (QWIPs), superlattice infrared photodetectors (SLIPs) have three different characteristics. The first one is the low operational bias. The electrons in the miniband of the superlattice (SL) are conductive while those in the quantum states of the multiple quantum wells (MQWs) are confined. The SL hence becomes a low resistance structure and thus no externally applied bias drops on the SL under low bias range. Therefore, the current blocking layer is needed to decrease the dark current in SLIPs and can determine the operational bias range.

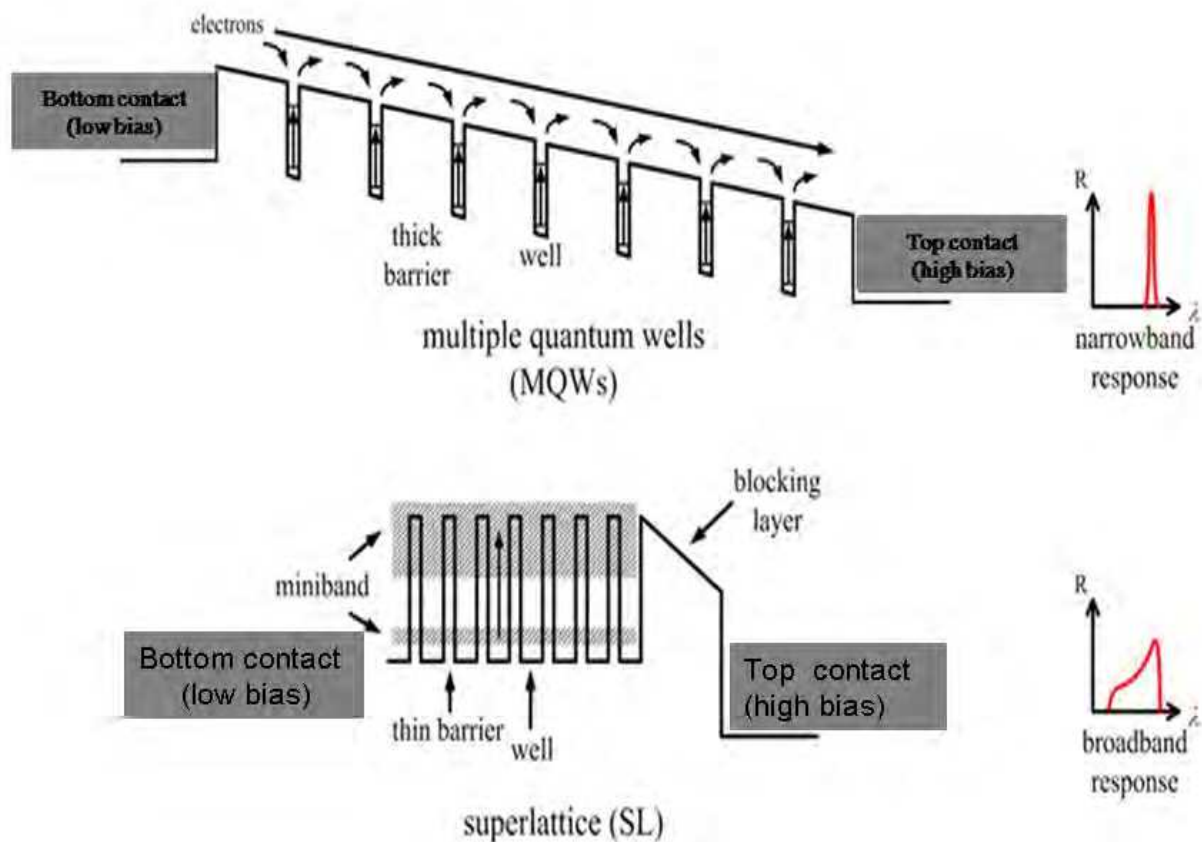


Fig. 1. The schematic band diagrams of multiple

We can design various structures of the blocking layers in order to reach the lower bias and less power consumption for operation. The second characteristic is broadband response of the SL. The transition type of SL is for a miniband to another miniband, so the absorption wavelength range is broader in comparison with QWIPs. Hence, the broadband detection can be done easily by using SL.

The third characteristic is voltage-tunable. We can design a proper current blocking layer to tune the absorption wavelength range of SLIPs with externally applied bias. Consequently, the functions of the blocking layer in SLIPs are not only to reduce the dark current but also to act as a bias-tuned energy filter. The above SLIP performances have been proved by our work (Chen et al., 2002) (Chen et al., 2003) (Lu et al., 2003). In particular, the voltage tunability will be explained in details in Sec 2.

In the detection of the thermal image, a focal plane array which is composed of the elements containing a detector and associated readout integrated circuit (ROIC). In order to avoid saturation of capacitance in ROIC, the low total current of the detector is necessary. In the MQW case, the photoexcited electrons need a high bias to transport through whole structure and contribute to the photocurrent, but the dark current increases dramatically under high bias. However, no externally applied bias drops on the SL under low bias range. The SL structure does not need a high bias to transport electrons. Lower biases and less power consumption can be achieved if the SLIP is chosen and the saturation of capacitance in ROIC can also be avoided.

Although detector performance is better when the temperature is lowered (Gumbs et al., 1994) (Jiang et al., 1999) (Majumdar et al., 2003), the cost for the liquid nitrogen cooling is

much cheaper than that for the liquid helium one. Therefore the detector has to be operated at the temperature higher than 77K. To achieve this goal for the SLIP, different blocking layers are needed to improve the operation temperature.

No. of detectors	structure descriptions	note
Detector 1	double SLs separating by a barrier	
Detector 2	one SLs sandwiched by double barriers(one 500nm thick and one 50nm thin barriers)	etched to emitter
Detector 3	one SLs sandwiched by double barriers (one 500nm thick and one 50nm thin barriers)	etched to SLs
Detector 4	one SLs with 50nm barrier	
Detector 5	one SLs and graded barrier with MQWs inserting	
Detector 6	one SLs with 300nm barrier	

Table 1.1. The descriptions of all detectors in this chapter

The principal goals of this chapter are the improvement of the responsivity and decrement of noise under low bias in order to increase the final detectivity and operation temperature. The demonstration of the flexibility with SL structure is also included in our principal goal. In the following sections, various SL structures and blocking layers are composed to become a detector with a specific principal goal. At first, a graded blocking layer is sandwiched between two different SLs to reach the multi-color detection which demonstrate the flexibility of the SL structure. Then double barriers with SL inserting are utilized to improve the responsivity. Next is the MQWs are integrated with the SLIP to act as a noise filter. Finally, the conclusion and future work will be discussed. Table 1.1 lists all the detectors shown in this chapter.

## 2 Multi-color Superlattices Infrared Photodetector

### 2.1 Introduction

In various applications such as aerospace observation, target discrimination and temperature sensing, an infrared photodetector for multi-color detection is essential. Because of the maturity and flexibility of band engineering, many works of intersubband multi-color infrared photodetectors have been devoted. The structures with quantum wells (Gravé et al., 1992) (Köck et al., 1992) (Martinet et al, 1992) (Tsai et al., 1993) (Liu et al., 1993) or superlattices (Hsu et al., 2000) (Chen et al., 2002) were reported to realize multi-color photodetectors.

In this section, we adopt two distinct superlattices separated by a blocking layer to achieve multi-color detection. The spectral responsivity of our photodetector is switchable between two wavelength regimes (6~8.5  $\mu\text{m}$  and 7.5~12  $\mu\text{m}$ ) by the bias polarity, and is also voltage-tunable in each wavelength regimes.

## 2.2 Sample Structure

Fig. 2.1 shows the band diagram of the double superlattice infrared photodetector and the corresponding energy levels. We denote this detector as Detector 1. The barrier height of the blocking layer is higher than the energy level of the bottom edge in the second mini-band of the superlattice. It is designed for the operation of the voltage tunability. In particular, the transitions of the electrons between the two miniband of the superlattice can be separately into the long-wavelength and the short-wavelength absorptions which correspond to the respective transitions from the top state of the first miniband into the bottom state of the second miniband and from the bottom state of the first miniband into the top state of the second miniband.

The structure contains sequentially a 400 nm top contact layer, a 14-period top superlattice, a blocking barrier, 14-period bottom superlattice, and a 500 nm bottom contact layer. Top superlattice is composed of 6 nm  $\text{Al}_{0.31}\text{Ga}_{0.69}\text{As}$  barrier and 4.5 nm GaAs well, and bottom one is composed 4 nm  $\text{Al}_{0.31}\text{Ga}_{0.69}\text{As}$  barrier and 6 nm GaAs well. The blocking barrier consists of a 60 nm  $\text{Al}_{0.27}\text{Ga}_{0.73}\text{As}$  layer, a 50 nm graded  $\text{Al}_x\text{Ga}_{1-x}\text{As}$  layer with  $x$  increasing from 0.27 to 0.31, and a 60 nm  $\text{Al}_{0.31}\text{Ga}_{0.69}\text{As}$  layer. Both superlattice wells and the contact layers are doped with  $1 \times 10^{18} \text{ cm}^{-3}$  of Si. The blocking barrier and the superlattice barriers are left undoped.

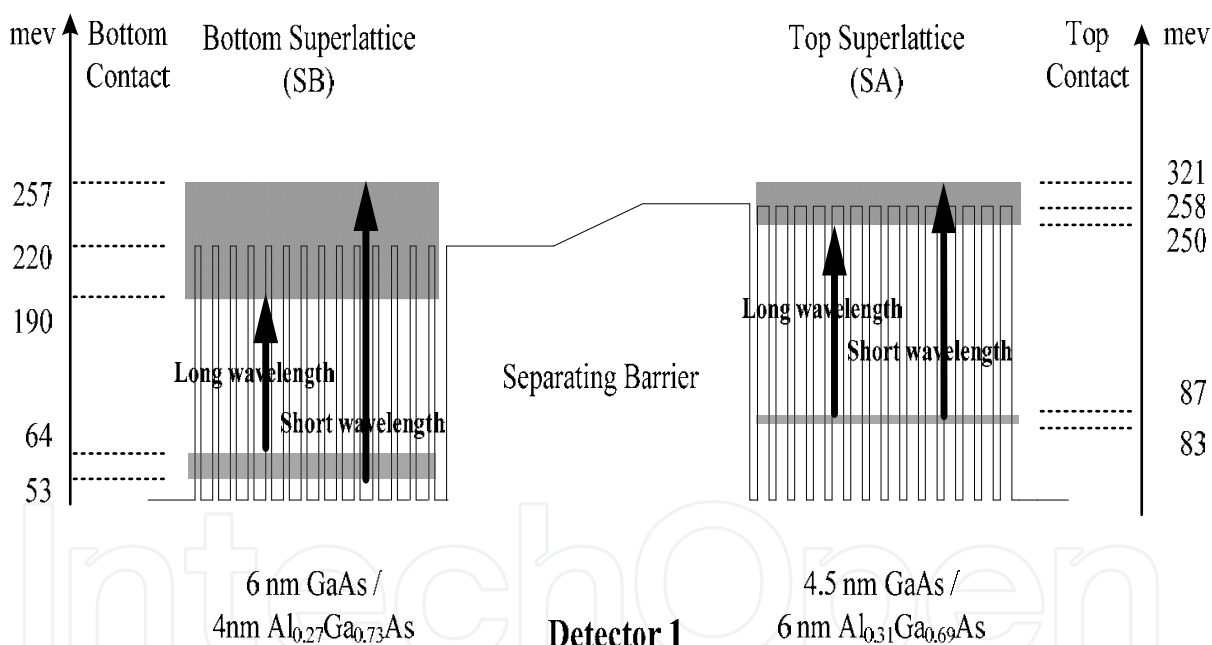


Fig. 2.1. The band diagram of Detector 1. It contains two superlattices and a separating barrier.

## 2.3 Operation Principle

To show the operation principles, the band structure under a positive bias is shown in Fig. 2.2. The voltage polarity is taken as positive if high potential is applied on the top contact. Because superlattices act as a low-resistance region, the applied voltage is almost totally dropped on the separating barrier. For convenience, we labeled top superlattices as superlattices A (SA), and the bottom one as superlattices B (SB). Under strong electric field applied on the barrier, the photoelectron in the second miniband of SB can tunnel through

the separating barrier. The escaped photoelectrons result in positive charges to attract electrons from the bottom contact and cause photocurrent in the external circuit.

On the contrary, the escaped photoelectrons in SA attract electrons from the top contact and result in internal current circulation as shown in Fig. 2.2. Therefore, only SB is active under positive bias. In the same way, only SA is active under negative bias. This characteristic makes the spectral responsivity switchable by the bias polarity between the two wavelength regimes corresponding to the respective miniband transition of SA and SB.

As shown in Fig 2.1, the barrier height of the blocking layer is actually a little bit higher than the energy level of the bottom edge in the second mini-band of the superlattice. This structure is designed for the operation of the voltage tunability. The operation principle for the voltage tunability in the superlattice with a single barrier is shown in Fig 2.3. The flat barrier of the blocking layer is assumed for the convenience to understand.

When the electron absorbs a photon to transit from the first miniband to the second miniband and become a photoelectron. The photoelectrons distributions corresponding to the second miniband energy are shown in the left and right insets of Fig 2.3 for long-wavelength and short-wavelength absorptions respectively. The insets under the same column are the same. For the long-wavelength absorption, the photoelectrons are always accumulated in the bottom state of the second miniband or relax into the first miniband as shown in the left inset. While for the short-wavelength absorption, most of the photoelectrons would relax from the top state of the second miniband into the bottom state or into the first miniband.

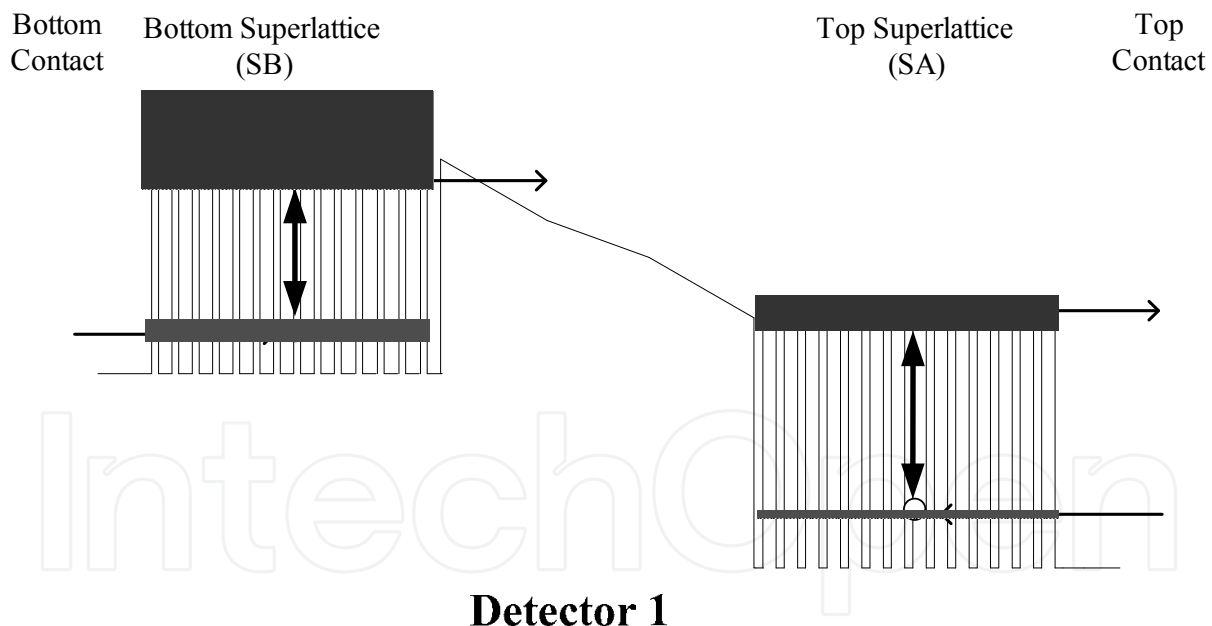


Fig. 2.2. The band diagram of Detector 1 under positive bias

Therefore, there are more photoelectrons in the bottom state than those in the top state as shown in the right inset. Fig 2.3 (a) and (b) demonstrate the tunneling behavior of the photoelectrons for the long-wavelength absorption under zero and high bias respectively, while Fig 2.3 (c) and (d) show the behavior of the photoelectrons for the short-wavelength absorption. For the long-wavelength absorption, especially under low bias, those photoelectrons which are accumulated in the bottom state of the second miniband can not

tunnel through the blocking layer as shown in Fig. 2.3 (a). When bias increases, for those photoelectrons, the tunneling path decreases and the associated tunneling photocurrent increases dramatically with tunneling probability increasing.

On the other hand for the short-wavelength absorption, photoelectrons with energy higher than barrier height can pass through the blocking layer even at zero bias as shown in Fig. 2.3 (c). As the applied bias increases, the number of photoelectrons, which can pass through the blocking layer, increases because of the increasing tunneling photoelectrons as shown in Fig. 2.3 (d).

In brief, under low bias, the photoelectrons generated by short wavelength radiation have higher energy and tunneling probability to contribute to the photoresponse. Short wavelength radiation dominates the spectral responsivity under low applied voltage. However, under high bias, the tunneling probability of the photoelectrons in the bottom state of the second miniband increases, and the long wavelength responsivity dominates the spectral responsivity. Fig. 2.4 is the schematic illustration of the responsivity under low bias, medium bias, and high bias. Under low bias, the responsivity is dominated by the short-wavelength absorption. Under medium bias, the responsivity for the short-wavelength and long-wavelength absorption are compatible. Under high bias, the responsivity is dominated by the long-wavelength absorption.

### Photoelectrons for long-wavelength radiation      Photoelectrons for short-wavelength radiation

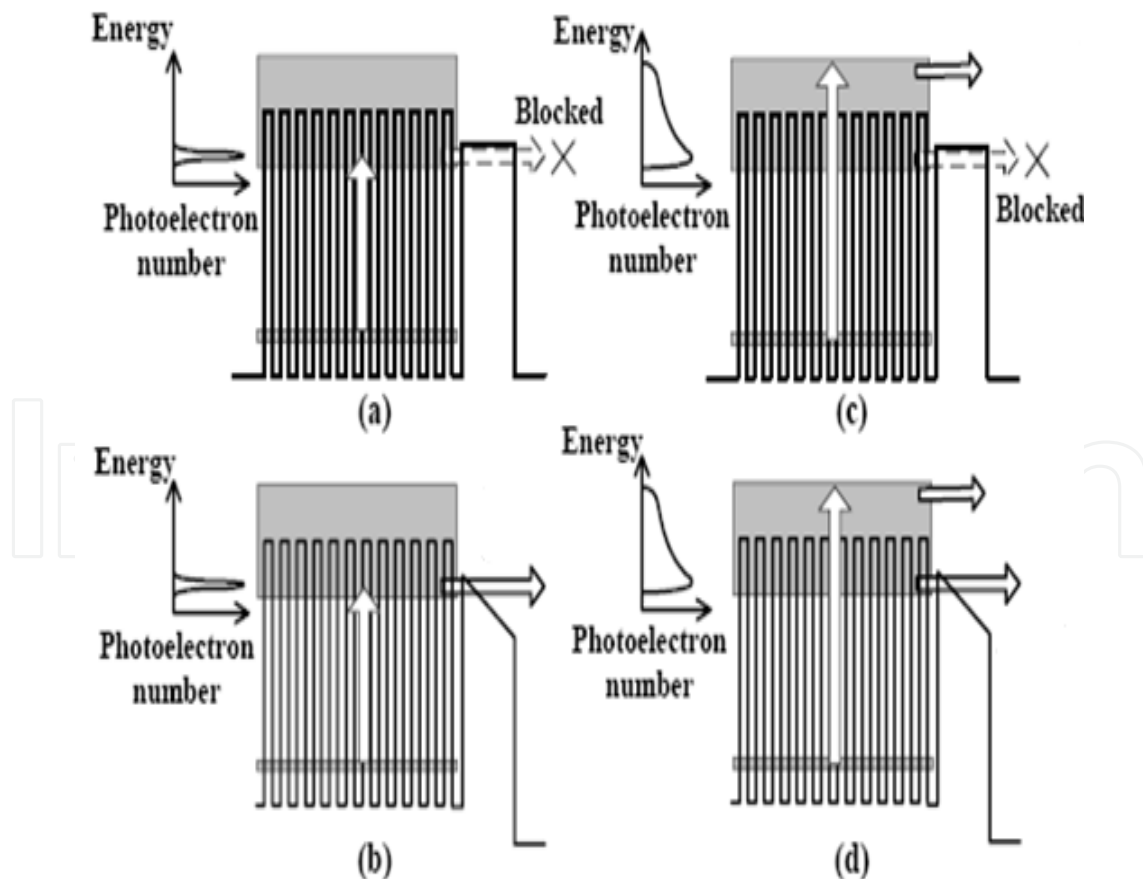


Fig. 2.3. Schematic illustration of photoelectron transport in a superlattice combined with a

blocking layer (a) under zero bias and illuminated by long-wavelength light (b) under high bias and illuminated by long-wavelength light. (c) under zero bias and illuminated by short-wavelength light (d) under high bias and illuminated by short-wavelength light. The distinct insets are the photoelectrons distribution corresponding to the second miniband energy for the long-wavelength and the short-wavelength absorption.

## 2.5 Responsivity

The measured spectral responsivity at 30 K is shown in Fig. 2.5. Under positive bias, only SB is active and dominates spectral responsivity, which is tunable in 7.5~12  $\mu\text{m}$  through the magnitude of the applied bias. Under negative bias, the spectral responsivity is dominated by the SA, and is also tunable in 6~8.5  $\mu\text{m}$ .

The theoretical calculation of the miniband as shown in Fig 2.1 demonstrates the short-wavelength and the long-wavelength absorptions for the SA happen at 5.2  $\mu\text{m}$  and 7.6  $\mu\text{m}$  and those for SB occur at 6  $\mu\text{m}$  and 9.8  $\mu\text{m}$ . The measured ones as show in Fig 2.5 are 6.8  $\mu\text{m}$  and 7.6  $\mu\text{m}$  for the short-wavelength and the long-wavelength absorptions of SA and 8.5  $\mu\text{m}$  and 9.8  $\mu\text{m}$  for the SB. The long-wavelength agrees very well but the short-wavelength does not. It is attributed to the relaxation of the most photoelectrons in the top states of the second miniband.

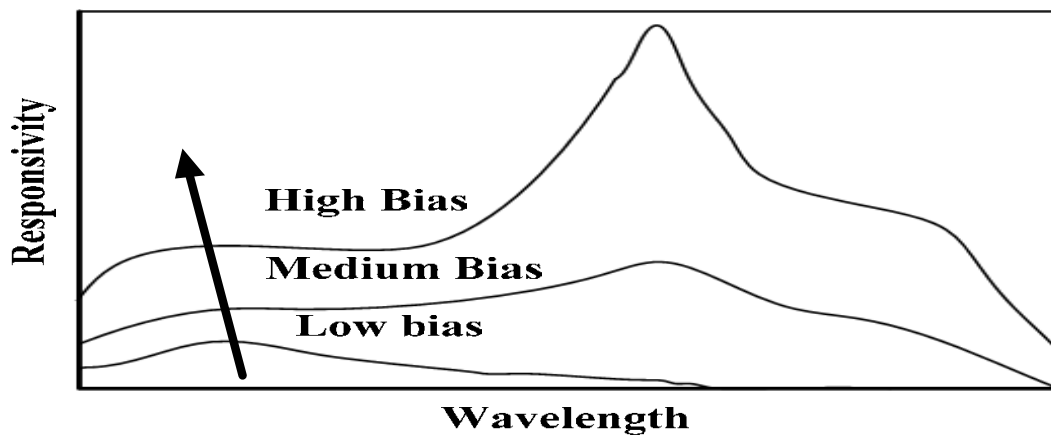


Fig. 2.4. Schematic illustration of the responsivity under low bias, medium bias, and high bias

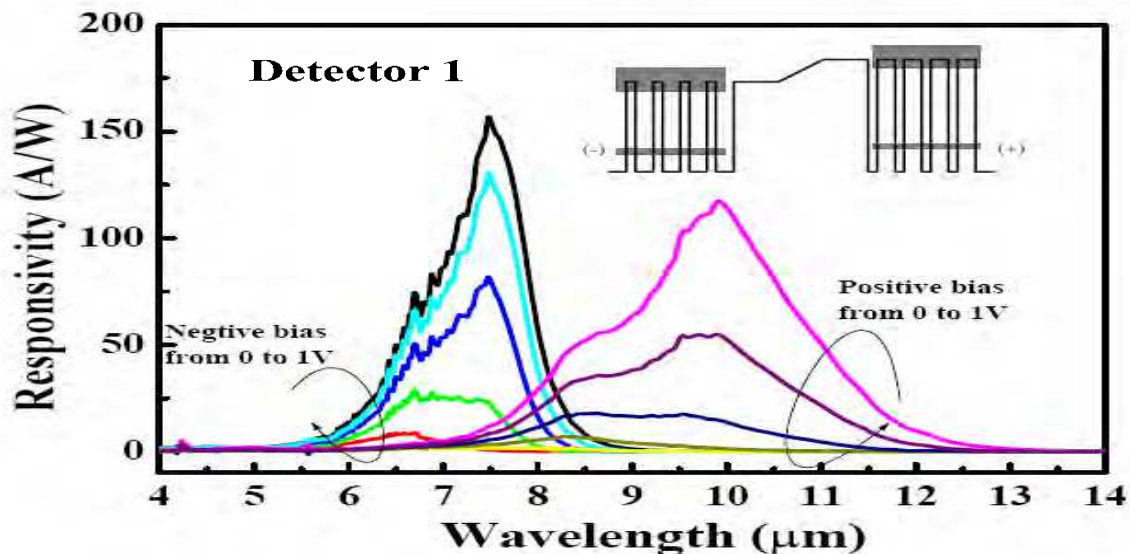


Fig. 2.5. The measured spectral responsivity at 30 K under several bias voltages

## 2.6 Detectivity

To evaluate the detectivity, the noise performance was measured from 1 to 8 kHz, which is limited by the noise and bandwidth of our amplifier. Under careful electrical and optical isolation, the current noise power spectral density at 77 K was measured with Detector 1 immersed in a 77 K liquid nitrogen dewar. With sophisticated calibration of the system noise, the detector noise under positive bias was extracted from the total measured noise, and is shown in Fig. 2.6. The noise of Detector 1 is white noise in the frequency range of our measurement system. Also shown in the inset of Fig. 2.6 are the measured noise data and the shot noise  $2eI_d$  calculated with the dark current at 77 K. The dashed line in the inset represents the estimated minimum resolvable noise of our noise measurement system.

It is observed that the measured noise PSD agrees with the estimated shot noise at 77 K for voltage larger than 0.5 V. Therefore, it is concluded that the noise source comes from the shot noise of the electrons tunneling through the blocking barrier. Since the dark current at 77 K under negative bias is much smaller than that under positive bias, it is not resolvable in our noise measurement system. In the following evaluation of detectivity, we assume the noise of our detector is also shot noise of the dark current. The zero background peak detectivity calculated with the shot noise of our detector is  $2.3 \times 10^{10} \text{ cmHz}^{0.5}/\text{W}$  at 50 K under 0.7 V with wavelength being 9.8  $\mu\text{m}$ , and is  $8.7 \times 10^{10} \text{ cmHz}^{0.5}/\text{W}$  at 70 K under -0.7 V with wavelength being 7.4  $\mu\text{m}$ .

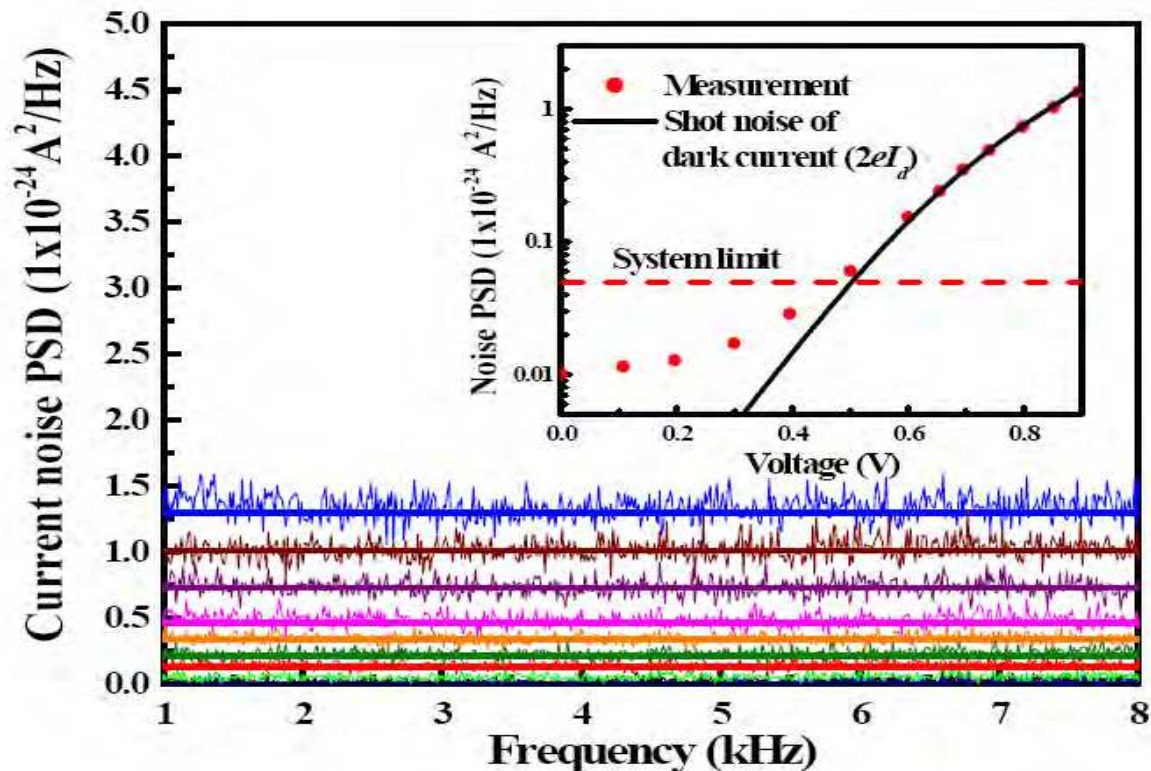


Fig. 2.6. The measured current PSD with the Detector 1 immersed in 77 K liquid nitrogen. Each line corresponds to each point in the inset. The solid curve represents the estimated shot noise calculated with the dark current at 77 K. The dashed line indicated the minimum resolvable noise of our measurement system.

## 2.7 Summary

In summary, we have designed and fabricated an infrared photodetector with two superlattices separated by a blocking barrier. The spectral responsivity of Detector 1 is tunable by the bias magnitude and is switchable by the bias polarities. These show that the structure is very appropriate to realize the multi-color infrared photodetector.

## 3. Double-Barrier Superlattice Infrared Photodetector

### 3.1 Introduction

An ordinary SLIP is realized by a SL structure with a single barrier. Because the SL is a low resistance structure, it is considered there is no applied bias dropped on the SL under the low bias. The photo-electrons in the second miniband of the SL can move either forward or backward (Chen et al., 2002) (Chen et al., 2003) (Lu et al., 2003). Some backward and escaping photo-electrons have no contribution to photocurrent. For the forward photo-electrons, the probability for those electrons to tunnel through the single barrier is assumed to be  $P$ . Those photo-electrons which move forward but can not tunnel through the barrier will finally relax into the first miniband. The total loss of photo-electrons is calculated to be  $(1 - P/2) \times 100\%$  and must be higher than 50%.

In order to solve this problem, we add a thick barrier into the left of this structure to increase the probability of bounce for photo-electrons in the second miniband. Then photo-electrons can have higher opportunity to tunnel through the thin barrier and contribute to photoresponse. This detector denoted by double-barrier superlattice infrared photodetector.

### 3.2 Sample structure

The sample structure of this detector from bottom to top is as following: a bottom contact layer, a 500 nm  $\text{Al}_{0.28}\text{Ga}_{0.72}\text{As}$  thick barrier, a 15-period SL, a 50 nm  $\text{Al}_{0.28}\text{Ga}_{0.72}\text{As}$  thin barrier and a top contact layer. Each period of the SL is composed of 6.5 nm GaAs well ( $N_d=2 \times 10^{17} \text{ cm}^{-3}$  Si) and 3.5 nm  $\text{Al}_{0.32}\text{Ga}_{0.68}\text{As}$  barrier (undoped). The sample was fabricated with the  $100 \mu\text{m} \times 100 \mu\text{m}$  square mesas then etched down to the bottom contact layer and evaporate metal onto the top of each mesa and the bottom contact. Hence, electrons must traverse the thick and thin barriers to generate the current. A  $45^\circ$  facet on the GaAs substrate is made to allow the TM polarized infrared light radiate on the photodetector to measure FTIR spectrum. The absorption wavelength range of the SL is about 6 to 10  $\mu\text{m}$ . The positive bias polarity is defined if high potential is applied on the top contact. Above device is denoted by Detector 2.

### 3.3 IV characteristic and excess electrons in the wells

The temperature-dependent current-voltage (I-V) curves of Detector 2 are shown in Fig. 3.1. The solid curves and the dashed curve are dark current at 50-100 K and photocurrent measured at 20 K under 300 K background radiations, respectively. A very asymmetric I-V curve is observed. The current magnitude of positive bias increases more dramatically than that of negative bias.

A possible mechanism qualitative to explain the dramatic asymmetry of the IV curve is shown in Fig. 3.2 (a) (b) and (c) which correspond to the negative, low positive, and high positive biases respectively. As bias magnitude increases, most of bias will drop on the thick barrier. Under the negative bias as shown in Fig. 3.2 (a), a small amount of positive ion charges appear in the left of the thick barrier due to the high doping density, a small amount of voltage drop is on the thin barrier. Electrons can be injected from the top contact through the thin barrier then relax onto SL. At the same time, the same amount of electrons is injected from SL through the thick barrier onto the bottom contact. No current component injected directly from the top contact through the SL into the bottom contact is expected to appear.

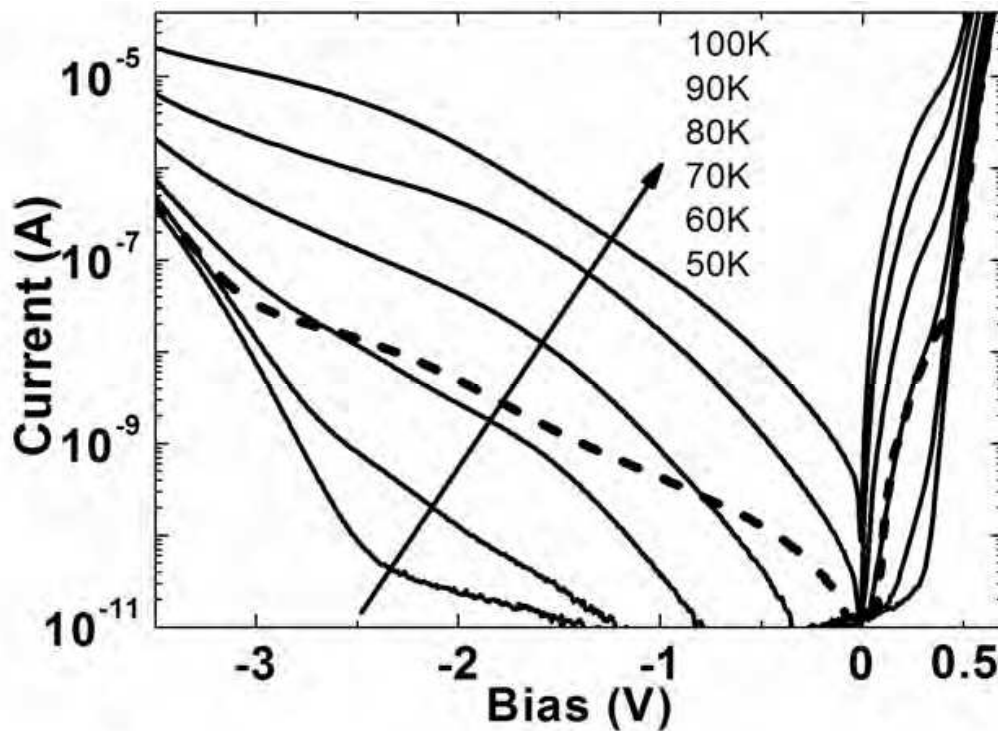


Fig. 3.1. (a) The dark current (solid lines) at different temperatures and the photocurrent (dashed line) versus the bias voltage of the Detector2.

On the other hand, under the positive bias as shown in Fig. 3.2 (b) and (c), the electrons in the SL near the thick barrier are repelled to move toward the thin barrier and a large amount of positive ion charges appear in this region due to the low doping density  $4 \times 10^{17} \text{ cm}^{-3}$  in SL compared with the doping density,  $1 \times 10^{18} \text{ cm}^{-3}$  in the contacts. A part of repelled electrons is expected to tunnel through the thin barrier and accumulate near the left side of the thick barrier through the external circuit as shown in Fig. 3.2 (b) and (c). The other part of repelled electrons will be trapped in the wells due to the breakdown of SL miniband. It is noted the SL still have miniband near the thin barrier. The trapped electrons are denoted as excess electrons in the wells. As bias increasing, the excess electrons in the wells tend to tunnel through the thin barrier. As bias is high enough, Fig. 3.2 (c) demonstrate the band diagram after the excess electrons all tunnel through the thin barrier.

In Fig. 3.2 (b), due to the misalign of the electron states in the wells under the region of positive electric field, the excess and doping electrons can not move toward the positive ion charges to neutralize them. A large negative field on the thick barrier produced by the positive ion charges and accumulating electrons at the bottom contact near the thick barrier renders the dark current to increase dramatically. Most of electrons injected from bottom contact through the thick barrier can be accelerated by positive ion charges and pass through the SL and thin barrier directly into the collector contact. Some electrons will relax into the SL and the same amount of electrons are injected through the thin barrier into the top contact. The amount of the electrons injected directly from the bottom contact into the top contact is expected to increase as the positive bias increases.

In addition in Fig. 3.2 (b), due to the positive electric field formed by the positive ion charges and excess electrons in the wells, the potential energy rise from the minimum point.

Therefore the total bias between the bottom and top contacts is about one tenth biases on the thick barrier. This can explain the asymmetry and the positive bias range is about ten times larger than negative bias range for the same current level. In other words, for the same magnitude of negative and positive biases, the dark current in positive bias is much larger than that under negative bias.

In order to solve this problem, we etch the sample down to SL to fabricate the metal contact on it directly instead of the bottom contact layer. We denoted this device as Detector 3 to differentiate from the above bottom contact sample Detector 2. Fig. 3.3 (a) and (b) show the band diagrams and the related cross-sectional plots of Detector 2 and Detector 3 respectively. For Detector 3, electrons escaped from the SL can be supplied from the metal contact immediately to overcome this problem and to improve the performance.

The I-V curves of Detector 3 at different temperatures are shown in Fig. 3.4. In comparison with the curves shown in Fig. 3.1, the operating bias range under both biases is symmetric. The inset shows the current comparison of Detector 2 and the Detector 3, it is observed that the Detector 3 has the lower dark current. Similar to the comparison of IV curve under positive and negative biases in Detector 2, it is attributed that no high injected current occur directly from the bottom contact to the top contact in Detector 3.

### 3.4 Responsivity and multiple bounce of the photoelectrons

The spectral responsivity under negative and positive biases of Detector 2 is shown in Fig. 3.5. (a),(b) respectively. For this spectra responsivity, the operational voltage ranges under positive and negative biases are consistent with the voltage range of I-V curve as shown in Fig. 3.1. The negative applied bias has to be ten times larger than that under positive bias for the same magnitude of responsivity. The spectral responsivities under positive bias of Detector 3 and 4 are shown in Fig. 3.5 (c) (d) respectively, where Detector 4 is a SLIP which has the same SL structure and single thin barrier. The applied bias ranges from 0.05 to 0.35V in both detectors. It is noted that the spectral responsivities of these four figures have the similar dependence on the bias with that as shown in Fig. 2.4. that is the short wavelength response appears under the low bias, the long wavelength response dominates under the high bias, and they are comparable under medium bias.

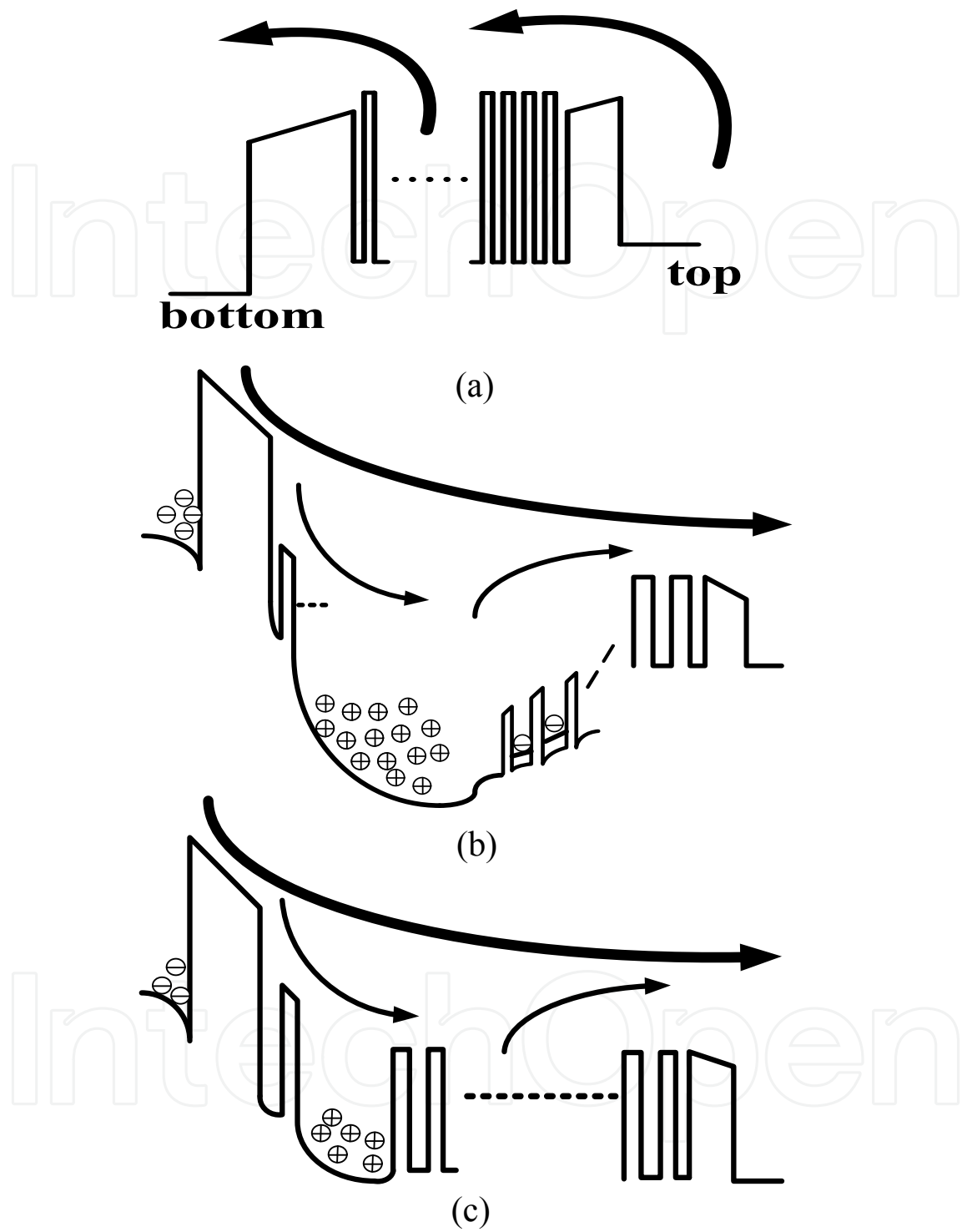


Fig. 3.2. Schematic illustration of band diagram of Detector 2 under (a) negative bias (b) low positive bias (c) high positive bias

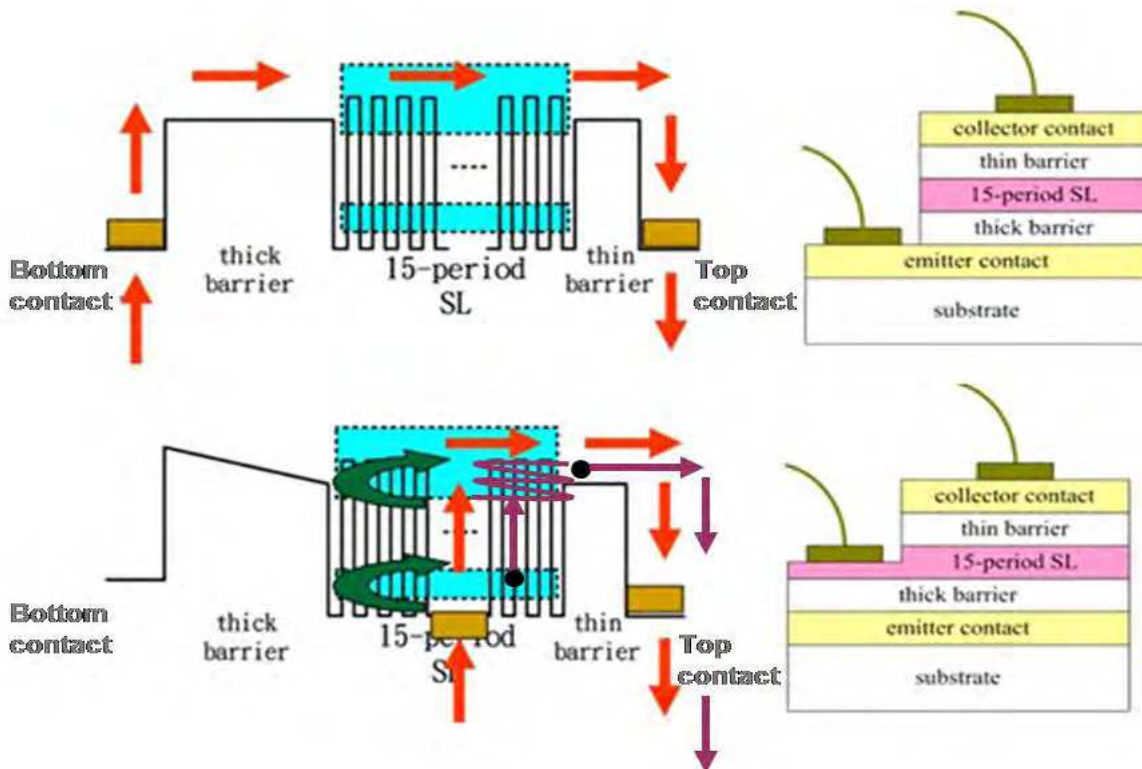


Fig. 3.3. The schematic band diagrams and the cross-sectional plots of (a) Detector 2 and (b) Detector 3. The arrows show the electron transport in these samples. For Detector 2, electrons have to transverse both of the barriers. However, in Detector 3, electrons have to transverse only the thin barrier.

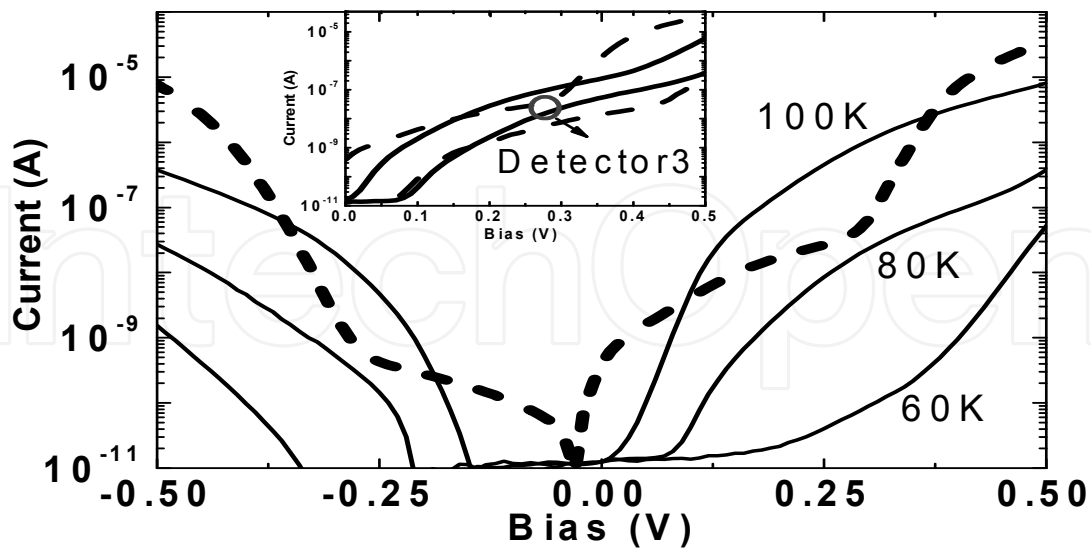


Fig. 3.4.(a) The dark current (solid lines) at different temperatures and the photocurrent (dashed line) versus the bias voltage of Detector 3. Inset shows the current comparison of Detector 2 and Detector 3. The solid lines and dashed line present the photocurrent and the dark current at 80K, respectively.

To further demonstrate the photocurrent improvement of Detector 3, the peak responsivities of Detectors 2, 3 and 4 at 80 K under several positive biases are shown in Fig. 3.6. Detector 3 has the higher responsivity than Detectors 2 and 4 under all applied biases. In particular at very low bias such as 0.15 V, the responsivity at 9.2  $\mu\text{m}$  of Detector 2, at 9.4  $\mu\text{m}$  of Detector 3 and at 9.2  $\mu\text{m}$  of Detector 4. It is noted that the responsivity of Detector 3 increases smoothly under all biases, but there are threshold voltages at 0.15V and 0.20V for the Detector 2 and 4 respectively. Especially under 0.15V, the responsivity of Detector 3 is at least ten times higher than those of Detectors 2 and 4. This is consistent with the comparison of the resulted background photocurrents of Detectors 2 and 3 shown in the inset of Fig. 3.4.

Under low positive bias, photoexcited electrons of Detector 3 can bounce several times in second miniband and enhance probability of tunneling through the thin barrier meanwhile the supply of electrons from the SL contact is no longer difficult as shown in Fig. 3.3(b). The similar hyperbolic shape of Detector 2 increases the threshold voltage of Detector 2 even to the higher bias than that of Detector 3. Under high positive bias, photoexcited electrons in second miniband of Detectors 3 and 4 can tunnel through the thin barrier at one time. So we can observe the responsivity difference between Detector 3 and 4 gradually decreased with bias increasing.

### 3.5 Detectivity

Because Detector 3 has the much higher responsivity about ten times than Detector 2 and Detector 4 at very low bias, its detectivity is also better in that range. Table 3.1 shows the comparison of detectivity at 80 K of the three detectors. It is observed that Detector 3 has the highest detectivity than the other detectors. The maximum detectivity value of Detector 3 is  $1.2 \times 10^{10} \text{ cmHz}^{1/2}/\text{W}$  for 9.4  $\mu\text{m}$  wavelength, which is higher than all of our previous works at 80K (Chen et al., 2002) (Chen et al., 2003). Therefore, the above analysis shows that the thick barrier is helpful to enhance the photoresponse, especially under low bias.

Detector number @ 80K	Wavelength	Detectivity ( $\text{cmHz}^{1/2}/\text{W}$ )
Detector 2	9.22 $\mu\text{m}$	$1.2 \times 10^9$
Detector 3	9.4 $\mu\text{m}$	$1.2 \times 10^{10}$
Detector 4	9.7 $\mu\text{m}$	$3.5 \times 10^9$

Table 3.1. Shows the comparison of detectivity at 80 K of the three detectors.

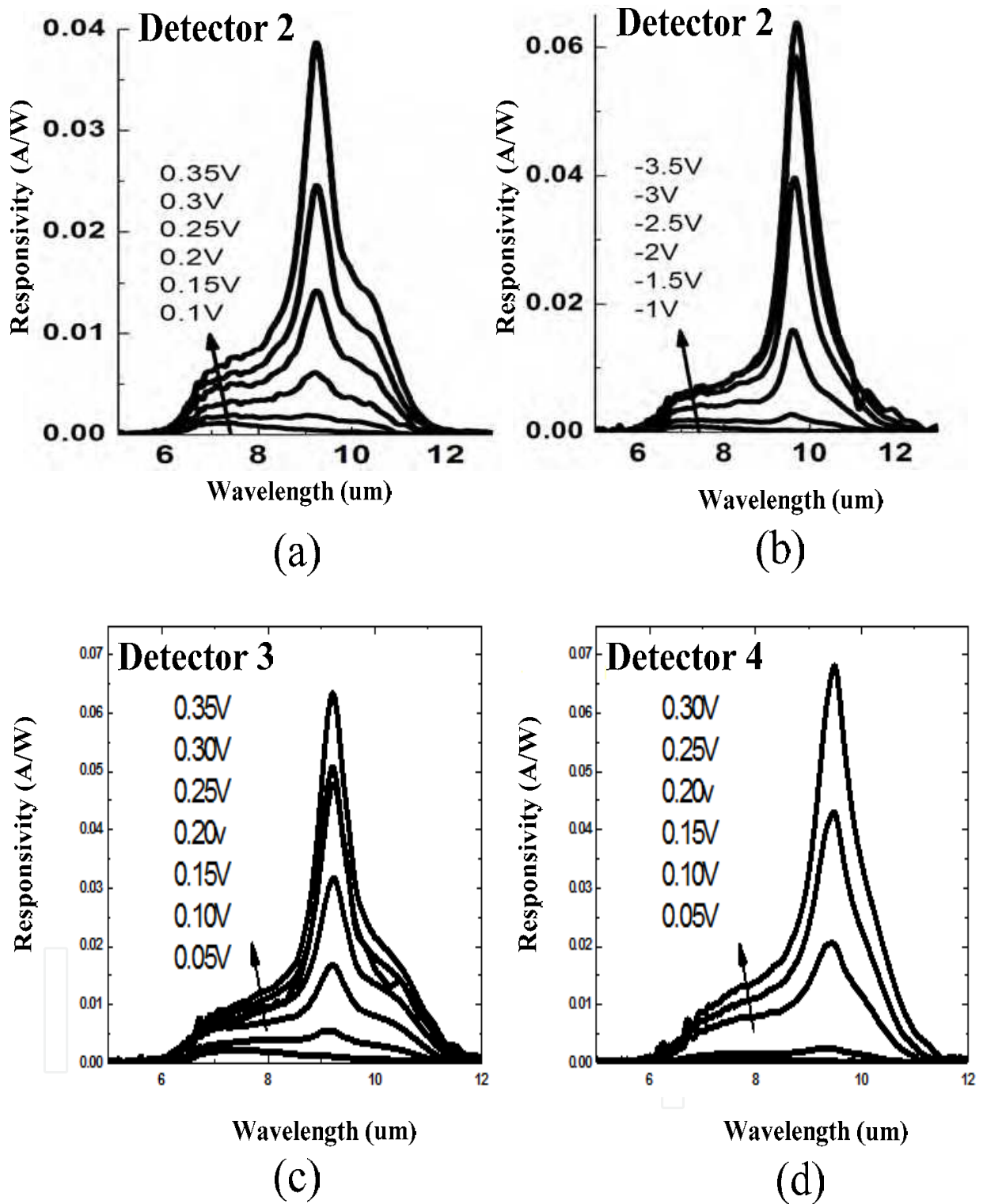


Fig. 3.5. (a) (b) The spectral responsivity of Detector 2 at 80 K under positive and negative bias respectively. (c) (d) The spectral responsivity of Detector 3 and 4 at 80 K under positive respectively.

### 3.6 Summary

We have investigated a double-barrier SLIP whose structure is a SL sandwiched between two asymmetric barriers. The thick and thin barriers can let the photoelectrons bounce several times in the second miniband of the SL to improve the responsivity dramatically at very low bias. However, the excess electrons trapped in the SL, the accumulating electrons at the bottom contact near the thick barrier and positive ion charges inside the SL result in high dark current under a small bias. A large electric field across the thick barrier makes the performance of the detector worse. The metal contact is fabricated directly onto the SL instead of the bottom layer to solve this problem. Detector 3 demonstrates higher responsivity under very low bias, although we demonstrate the responsivity at 80K yet it can be operated at 100K. Detector 3 also shows the higher responsivity at 80k than our previous works for the Detector 4.

## 4. The SLIP integrated with MQWs

### 4.1 Introduction

In order to reduce the dark current and noise power under low bias, an ordinary SLIP with a thin barrier followed by additional MQWs has been developed as shown in Fig. 4.1. The whole structure can be divided into two parts. The SL is used as an active region for the primary photoresponse while the MQWs are considered as a noise filter for noise reduction. Because of the high capture probability of the wells for the electrons under low bias, almost all electrons traversing a barrier are recaptured into the neighboring well. The photoelectrons and dark electrons from the SL are hence recaptured in the first well of the MQWs and produce the capture current. This current must be balanced by the emission current from the well under steady state due to the charge neutrality. It assures that the total current, especially the photocurrent generated from SL can also flow through the whole structure without loss under low bias as indicated by the arrows in Fig. 4.1.

Furthermore, MQWs are capable of providing additional photocurrent to improve photoresponse under low-voltage operation.

Because of thermally assisted tunneling of the electrons through the barrier, the noise of the SLIP with a single barrier is proved in Fig 2.6 as shot noise:

$$i_{SB}^2 = 2eI_D$$

where  $i_{SB}$  is the noise current power spectral density (PSD) of the SLIP and  $I_D$  is the dark current. On the other hand, the noise of MQWs is the generation-recombination noise.

$$i_{QW}^2 = 4eg_n I_D \text{ and } g_n = 1/(N p_c)$$

where  $i_{QW}$  is the noise current PSD of the MQWs,  $g_n$  is the noise gain of MQWs,  $I_D$  is the dark current, and  $N$  is the number of wells. The  $p_c$  is the capture probability of the single well and is approximately 1 under low bias when the noise gain is the smallest as indicated by the downward arrows in Fig. 4.1. The total noise current PSD of the combination of SLIP with MQWs is still the generation and recombination noise since their current always passes through the MQWs. Without the loss of the photocurrent from the SL, the MQWs can act as a noise filter under the low bias.

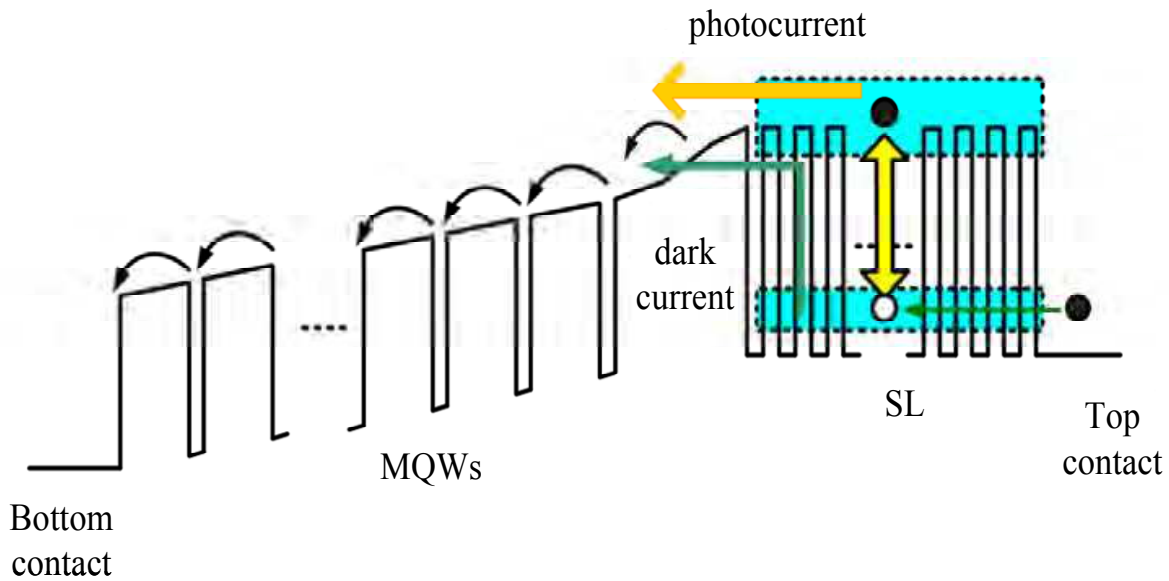


Fig. 4.1. The band diagram of SL integrated with MQWs.

#### 4.2 Sample Structure

For the comparison of the differences between SLIP and SLIP with MQWs, Detector 5 and Detector 6 are designed. The structure of Detector 5 from top to bottom is as follows: a contact layer, a SL, a 60 nm  $\text{Al}_x\text{Ga}_{1-x}\text{As}$  graded barrier, a 50-period MQWs and a contact layer. Detector 6 is a SL with a single barrier sandwiched between two contact layers. The single barrier is a 300 nm  $\text{Al}_{0.25}\text{Ga}_{0.75}\text{As}$  layer. For the MQWs, each period consists of 6nm GaAs well ( $n = 4 \times 10^{17} \text{ cm}^{-3}$ ) and 50nm  $\text{Al}_{0.21}\text{Ga}_{0.79}\text{As}$  barrier (undoped). And each period of the SL consists of 6nm GaAs well ( $n = 4 \times 10^{17} \text{ cm}^{-3}$ ) and 4nm  $\text{Al}_{0.29}\text{Ga}_{0.71}\text{As}$  barrier (undoped).

#### 4.3 Noise gain

It is clearly that if  $gn$  is less than 0.5, the noise of SLIP with MQWs is lower in comparison with an ordinary SLIP. Fig. 4.2 shows the measured noise gain of SLIP with 50-period MQWs. It is noted that the noise gain is very small under the low bias range. For example,  $i_{QW}^2$  can be 50 times less than  $i_{SB}^2$  at 0.01V. It is the reason why the SLIP with MQWs is appropriate for the operation at low bias as mentioned above.

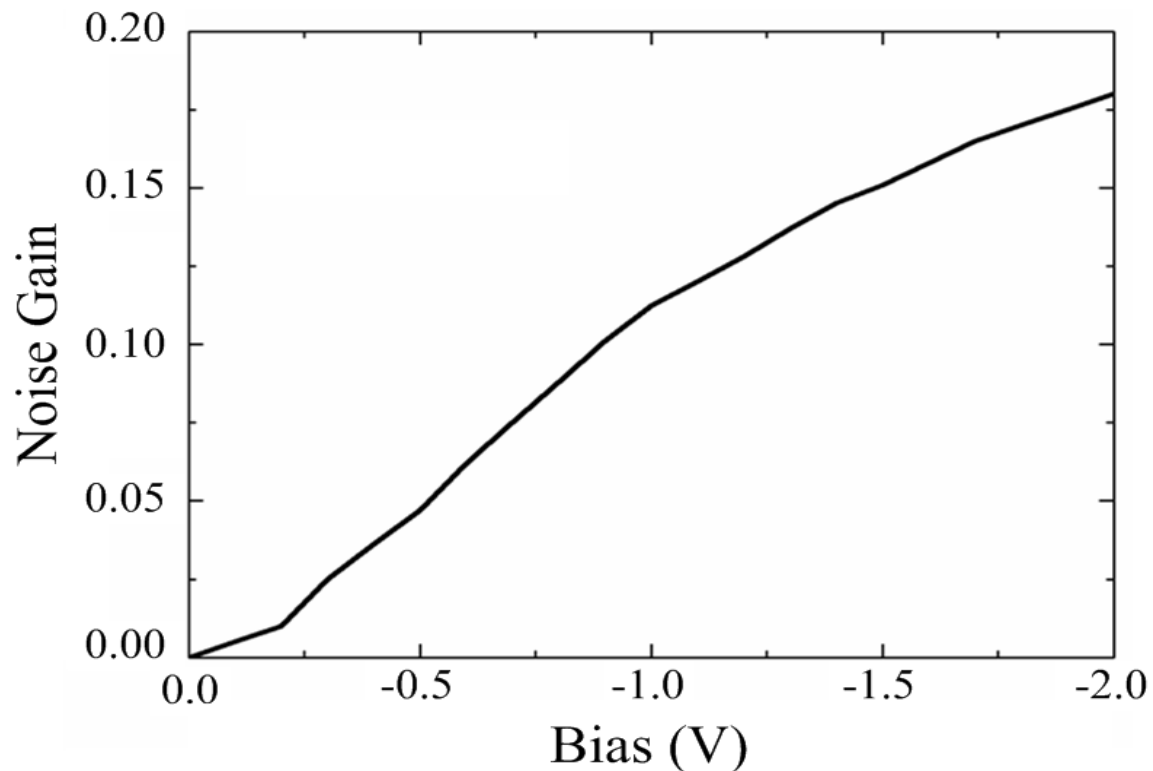


Fig. 4.2. The noise gain of SL integrated with MQWs under negative bias at 80 K.

#### 4.4 Responsivity

Fig. 4.3 shows the photoresponse of Detector 5 at 80K with different biases. The line without solid squares is for the positive bias on the top contact and the other one is for the negative bias. Based on the band diagram in Fig. 4.1, only the MQWs are active under the positive bias while both the SL and MQWs are active under the negative bias.

As shown in the Fig. 4.3, it is obvious that the responsivity magnitude increases with the bias magnitude for both bias polarities. By comparing the spectral range for both bias polarities, it is concluded that the SL has a responsivity peak at  $7.4\mu\text{m}$  which correspond to short wavelength absorption in the SL structure and the MQWs have a peak at  $11.4\mu\text{m}$ . Especially the responsivity for the MQWs increases quickly under the positive bias range but less than or compatibly with the SL one under the negative bias range. Therefore it is expected that the SLIP with the MQWs can be operated under 0V to -0.7V. In particular, the SL responsivity is dominant for 0V to -0.3V which the noise gain is also very small.

Fig. 4.4 shows the responsivity of Detector 5 under -0.2V bias at 40K, 60K and 80K. The responsivity spectral range is actually compatible with 300K blackbody radiation spectrum which is sketched as the dotted curve. For the responsivity, the functions of the MQWs are not only to act as a noise filter but also to enhance the long wavelength response for broadband detection.

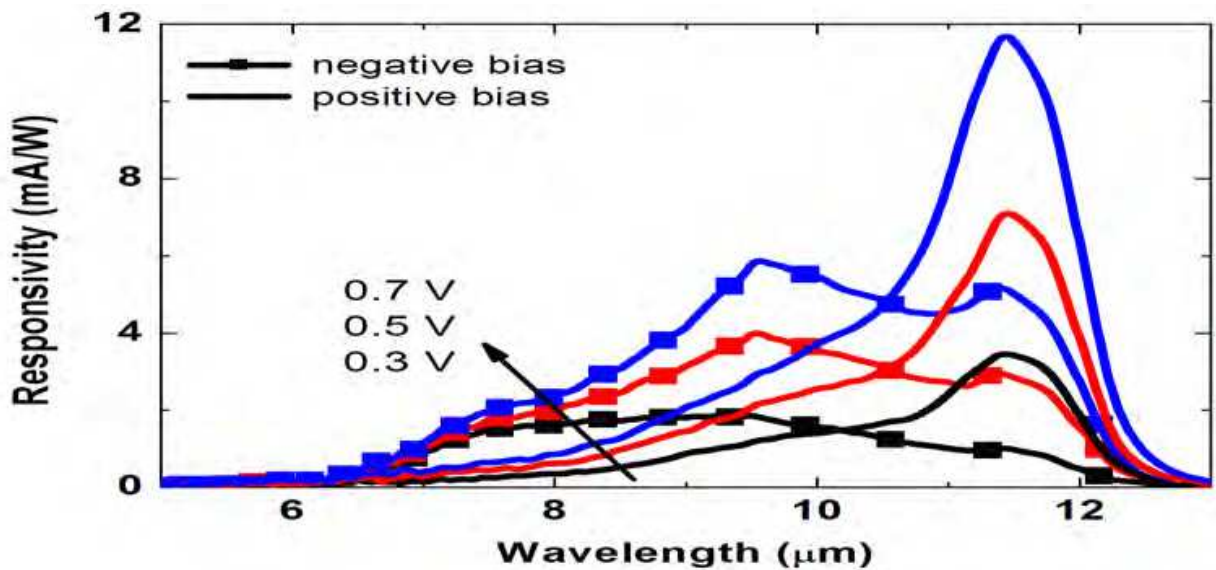


Fig. 4.3. The photoresponse comparison of Detector 5 under different positive and negative biases at 80 K. It is observed that the response spectra under negative bias are more broadband and flatband than those under positive bias.

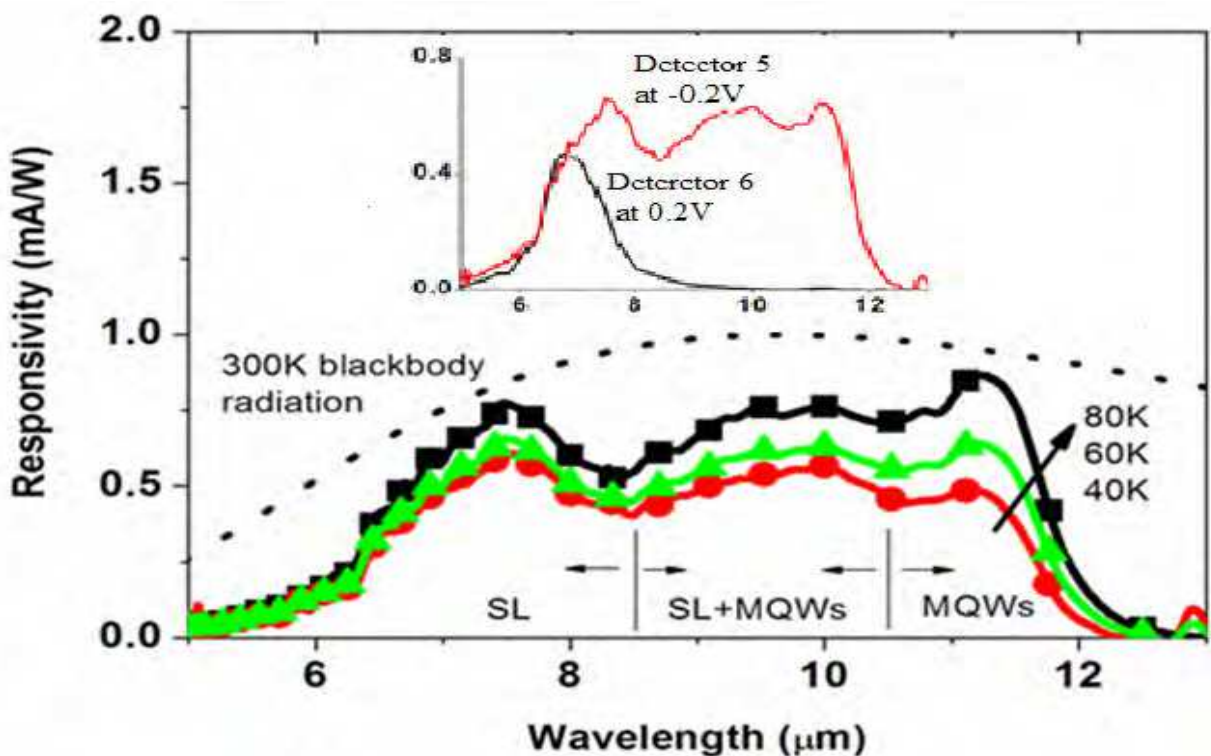


Fig. 4.4. The photoresponse of Detector 5 under -0.2 V at different temperatures. Its detection range is compatible with the intensity distribution of 300 K blackbody radiation which is sketched as the dotted line (not in scale). The inset shows the response of Detector 5 at -0.2 V and that of Detector 6 at 0.2 V

The reason why the responsivity increases a little bit with the temperature rising is attributed to the low doping density of  $4 \times 10^{17} \text{ cm}^{-3}$  in the wells of the SL and MQWs. Some

of the electrons are frozen in the impurity states in the wells. As the temperature rises, they can escape from the impurity states into the well to improve the responsivity. This freezing effect actually becomes the less at the higher temperature. Comparing Detector 1 in sec2 and Detector 5 in this sec, the responsivity of Detector 1 is temperature independent because of high doping density in the wells and no freezing effect occur. In additions, the advantage for the low doping density is to decrease the dark current in order to improve the detector operation at the high temperature.

In the inset of Fig. 4.4, the responsivity comparison between Detector 5 and Detector 6 is demonstrated. The bias is given under the same electric field on the blocking layer in the two samples. It is obvious that Detector 5 has a broader spectrum than Detector 6 due to the additional contribution of the MQWs.

#### 4.5 Detectivity

Fig. 4.5(a) shows the detectivity ( $D^*$ ) of Detector 5 under positive and negative biases at 50K, 60K, 80K. Detector 5 consists of SL and MQWs, the responsivities for the wavelength 11.7  $\mu\text{m}$ (MQW peak) and 7.4  $\mu\text{m}$ (SL peak) were chosen respectively to calculate the  $D^*$  under positive and negative biases. Under negative bias, as bias magnitude decrease from -0.7V the  $D^*$  increase quickly. On the other hand, under the positive bias, the  $D^*$  decrease when the bias magnitude decrease from 0.7V. It is attributed to the additional contribution of the SL responsivity under the low negative bias except the contribution of MQWs.

Despite the small SL responsivity under the low negative bias, both the corresponding dark current and the noise gain are low enough to make  $D^*$  increase as the bias magnitude decreases. Hence the maximum  $D^*$  under positive bias (MQWs) is still less than maximum  $D^*$  under negative bias (SL+MQWs) at the same temperature. Fig. 4.5(b) shows the comparison of  $D^*$  between Detectors 5 and 6 for 7.4  $\mu\text{m}$ . The  $D^*$  under negative and positive biases represents the respective performance for the Detectors 5 and 6. The  $D^*$  of Detector 5 is better than that of Detector 6 under the same bias magnitude for any temperature although they have similar responsivity. It is attributed to the different noise performance i.e., generation-recombination noise and shot noise for Detectors 5 and 6 respectively.

#### 4.6 summary

The SL integrated with the MQWs shows low noise, and broadband response under the low bias. In comparison with MQWs, the additional contribution of SL responsivity renders the better performance in our detector. In comparison with ordinary SLIP, the MQW in our detector shows better noise performance. Therefore this detector is appropriate for operation under the low biases and high temperature ( $\geq 80\text{K}$ ).

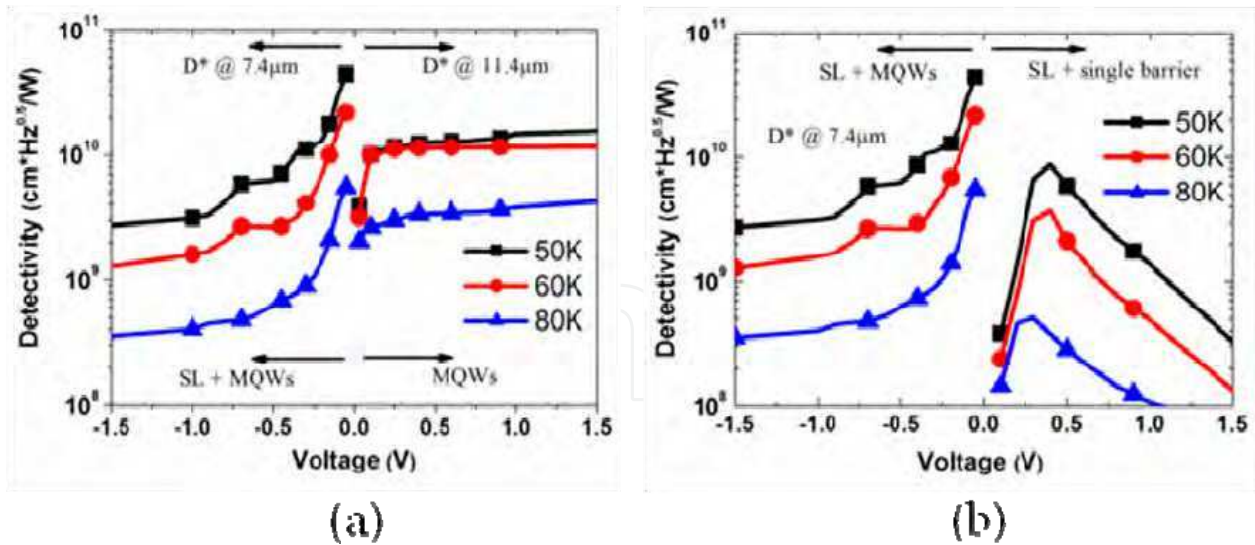


Fig. 4.5. (a) The detectivity ( $D^*$ ) of Detector 5 versus voltage at 50 K, 60 K and 80 K under  $7.4\mu\text{m}$  and  $11.4\mu\text{m}$ . Because the photoresponse comes from the different structures, the corresponding  $D^*$  wavelengths under positive and negative bias are  $11.4$  and  $7.4\mu\text{m}$ , respectively. (b) The comparison of  $D^*$  at  $7.4\mu\text{m}$  between Detector 5 and Detector 6.

## 5. The conclusion and future work

Various SL structures and blocking layers are combined to form a detector with a specific application. At first, a blocking barrier separated two distinct superlattices was made to obtain the multi-color detection which demonstrate the flexibility of the SL structure. In comparison with the conventional multicolor photodetectors, the double-superlattice photodetectors show advantages including temperature invariance of the spectral responsivity, the flexibility for the design of a multicolor photodetector and the same order of responsivities in the two different wavelength regions. But the main disadvantage is its low operational temperature. It is also noted the noise performance of such SLIPs belongs to shot noise compared with generation-recombination noise of the QWIPs the shot noise actually higher than generation-recombination noise under the low bias. For a detector operated under the low bias, the noise performance should be improved.

In order to increase the operation temperature, we design the double barriers with SL inserting. The additional thick barrier compared to ordinary SLIP is used to bounce electrons backward to enhance the photoresponse. However, the dark current increase dramatically under low bias and threshold voltage of photocurrent is postponed. The possible model is given to explain this phenomenon inside the SL the excess electrons trapped in the wells and positive ion charges near the thick barrier form a large electric field to reduce the potential bias. At the same time, the accumulating electrons in the contact near the thick barrier and positive ion charges inside the SL form a large electric field to increase dark current dramatically. To solve this problem, the metallic contact is made on the SL instead of the bottom contact. For this detector, we observe a higher responsivity than the ordinary SLIP which has only one thin barrier. The thick barrier can really enhance the photoresponse of SL, especially under low bias. The resulted operation temperature for this detector is higher than 80K.

To improve noise performance under low bias, we further design a SL followed by a

multiple quantum wells (MQWs). The MQWs are used to reduce the noise current power and add the response range. The noise gain of generation and combination noise is very small under low bias compared to the shot noise. On the other hand, the SL is utilized to inject the photocurrent into the QWIPs under low bias. In fact, the photocurrent of the SL is not reduced by the MQWs. As the result, this detector has the higher  $D^*$  than the ordinary SLIP and QWIP, at the temperature of 80K.

The double-superlattice infrared photodetectors show multicolour detection and the flexibility of SL structure while the double-barrier superlattice infrared photodetectors and the SLIP integrated with MQWs can be operated at high-temperature with high detectivity. The combination of quantum well infrared photodetector (QWIP) and double-barrier SLIP will be completed in the future. Even the operating temperature is expected to be above 100K with high detectivity. Such kind of SLIP is promising candidate of a pixel in the focal plane array especially such detector would not saturate the capacitor in ROIC because of the low dark current under low bias.

## 6. Acknowledgement

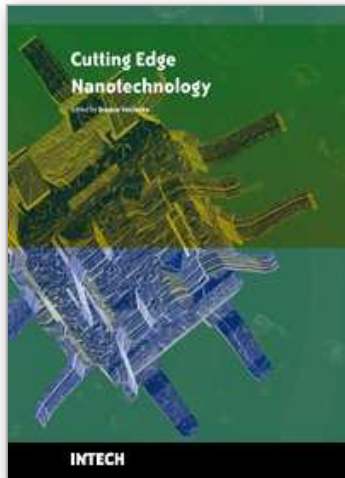
This work was supported by National Science Council of ROC under contract No. NSC 97-2221-E-002-053-MY3.

## 7. References

- A. S. Sedra, and K. C. Smith, "Microelectronic Circuits", Oxford University Press, USA, 4 edition, ch. 4
- B. F. Levine (1993). Restore Desktop View
- C. C. Chen, H. C. Chen, C. H. Kuan, S. D. Lin, and C. P. Lee (2002). Multicolor infrared detection realized with two distinct superlattices separated by a blocking barrier. *Appl. Phys. Lett.* 80, 2251.
- C. C. Chen, H. C. Chen, M. C. Hsu, W. H. Hsieh, C. H. Kuan, S. Y. Wang, and C. P. Lee (2002). Performance and application of a superlattice infrared photodetector with a blocking barrier. *J. Appl. Phys.* 91, 943.
- Chen, C. Y. & Kuan C. H. (2000). Design and calibration of a noise measurement system. *IEEE T.I.M.* , 77, 49
- Gravé, I. ; Shakouri, A. ; Kuze, N. & Yariv, A. (1992). Voltage-controlled tunable GaAs/AlGaAs multistack quantum well infrared detector. *Appl. Phys. Lett.* , 60, 2362
- Gumbs, G. ; Huang, D. & Fessatidis, V. (1994). Many-body effects on temperature dependence of the interband absorption in quantum wells. *J. Appl. Phys.* , 75, 7942
- Gunapala S. D. et al. (2000). 640×486 long-wavelength two-color GaAs/AlGaAs quantum well infrared photodetector (QWIP) focal plane array camera. *IEEE T-ED*, 47, 963
- Harwit, A. & Harris Jr., J. S. (1987). Observation of Stark shifts in quantum well intersubband transitions. *Appl. Phys. Lett.* , 50, 685
- Hsu, M.C. ; Kuan, C.H. & Wang, S. Y. (2000). Multicolor infrared detection using two stacks of superlattice structures in a back-to-back configuration. *Appl. Phys. Lett.* , 77, 2240

- J. H. Lu, Y. Y. Yang, C. C. Chen, C. H. Kuan, H. T. Chen, and S. C. Lee (2003). Study of period number effect in the superlattice infrared photodetector. *Infra. Phys. & Technol.* 44, 399.
- Jiang, X. D. ; Li, S. S. & Tidrow, M. Z. (1999). Investigation of a multistack voltage-tunable four-color quantum-well infrared photodetector for mid- and long-wavelength infrared detection. *IEEE J. Quant. Electron.* , 35, 1685
- K. K. Choi, "The Physics of Quantum Well Infrared Photodetectors," World Scientific, River Edge, NJ, 1997, pp.294
- Köck, A. ; Gornik, E. ; Abstreiter, G. ; Böhm, G. ; Walther, M. & Weimann, G. (1992). Double wavelength selective GaAs/AlGaAs infrared detector device. *Appl. Phys. Lett.* , 60, 2011
- Levine, B. F. ; Choi, K. K. ; Bethea, C. G. ; Walker, J. & Malik, R. J. (1987). New 10  $\mu\text{m}$  infrared detector using intersubband absorption in resonant tunneling GaAlAs superlattices. *Appl. Phys. Lett.* , 50, 1092
- Liu, H. C. ; Li, J. ; Thompson, J. R. ; Wasilewski, Z. R. ; Buchanan, M. & Simmons, J. G. (1993). Multicolor voltage-tunable quantum-well infrared photodetector. *IEEE Elect. Dev. Lett.* , 14, 566
- Lu, J. H. ; Yang, Y. Y. ; Chen, C. C. ; Kuan, C. H. ; Chen H. T. & Lee, S. C. (2003). Study of period number effect in the superlattice infrared photodetector. *Infra. Phys. & Technol.* , 44, 399
- Majumdar, A. ; Choi, K. K. ; Rokhinson, L. P. & Tsui, D. C. (2003). Temperature dependence of electron transfer in coupled quantum wells. *Appl. Phys. Lett.* , 82, 686
- Martinet, E. ; Rosencher, E. ; Luc, F. ; Bois, Ph. ; Costard, E. & Delaître, S. (1992). Switchable bicolor (5.5–9.0  $\mu\text{m}$ ) infrared detector using asymmetric GaAs/AlGaAs multiquantum well. *Appl. Phys. Lett.* , 61, 246
- Tsai, K. L. ; Chang, K. H.; Lee, C. P. ; Huang, K. F. ; Tsang, J. S. & Chen, H. R. (1993). Two-color infrared photodetector using GaAs/AlGaAs and strained InGaAs/AlGaAs multiquantum wells. *Appl. Phys. Lett.* , 62, 3504
- West, L. C. & Eglash, S. J. (1985). First observation of an extremely large-dipole infrared transition within the conduction band of a GaAs quantum well. *Appl. Phys. Lett.* , 46, 1156

IntechOpen



## **Cutting Edge Nanotechnology**

Edited by Dragica Vasileska

ISBN 978-953-7619-93-0

Hard cover, 444 pages

**Publisher** InTech

**Published online** 01, March, 2010

**Published in print edition** March, 2010

The main purpose of this book is to describe important issues in various types of devices ranging from conventional transistors (opening chapters of the book) to molecular electronic devices whose fabrication and operation is discussed in the last few chapters of the book. As such, this book can serve as a guide for identifications of important areas of research in micro, nano and molecular electronics. We deeply acknowledge valuable contributions that each of the authors made in writing these excellent chapters.

### **How to reference**

In order to correctly reference this scholarly work, feel free to copy and paste the following:

Shih-Hung Lin, Ying-Hsiang Wang, Che-Wei Chang, Jen-Hsiang Lu, Chun Chi Chen and Chieh-Hsiung Kuan (2010). Development of Superlattice Infrared Photodetectors, Cutting Edge Nanotechnology, Dragica Vasileska (Ed.), ISBN: 978-953-7619-93-0, InTech, Available from: <http://www.intechopen.com/books/cutting-edge-nanotechnology/development-of-superlattice-infrared-photodetectors>

**INTECH**  
open science | open minds

### **InTech Europe**

University Campus STeP Ri  
Slavka Krautzeka 83/A  
51000 Rijeka, Croatia  
Phone: +385 (51) 770 447  
Fax: +385 (51) 686 166  
[www.intechopen.com](http://www.intechopen.com)

### **InTech China**

Unit 405, Office Block, Hotel Equatorial Shanghai  
No.65, Yan An Road (West), Shanghai, 200040, China  
中国上海市延安西路65号上海国际贵都大饭店办公楼405单元  
Phone: +86-21-62489820  
Fax: +86-21-62489821

© 2010 The Author(s). Licensee IntechOpen. This chapter is distributed under the terms of the [Creative Commons Attribution-NonCommercial-ShareAlike-3.0 License](#), which permits use, distribution and reproduction for non-commercial purposes, provided the original is properly cited and derivative works building on this content are distributed under the same license.

IntechOpen

IntechOpen